Electronic Supplementary Information

A Hierarchically Porous Nickel-Copper Phosphide Nano-Foam for Efficient Electrochemical Splitting of Water

Li Wei[a], Kunli Goh[b], Özgür Birer[c], H. Enis Karahan[b], Shengli Zhai[a,b], Xuncai Chen[a], and Yuan Chen[a,*]

a. The University of Sydney, School of Chemical and Biomolecular Engineering, Sydney, New South Wales, 2006, Australia.

*Email address: yuan.chen@sydney.edu.au

b. Nanyang Technological University, School of Chemical and Biomedical Engineering, 637459, Singapore.

c. Koç University, Chemistry Department and KUYTAM Surface Science and Technology Center, Rumelifeneri Yolu, Sarıyer, 34450, Istanbul, Turkey

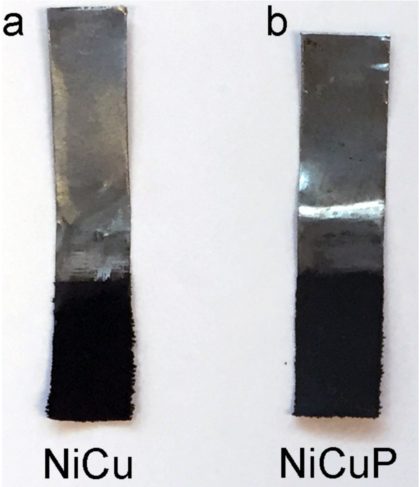

Figure S1. Photographs of stainless steel electrodes deposited with (a) NiCu alloys and (b) phosphidized NiCuP catalysts. The deposited electrode area is about 0.5 × 1.0 cm^2.

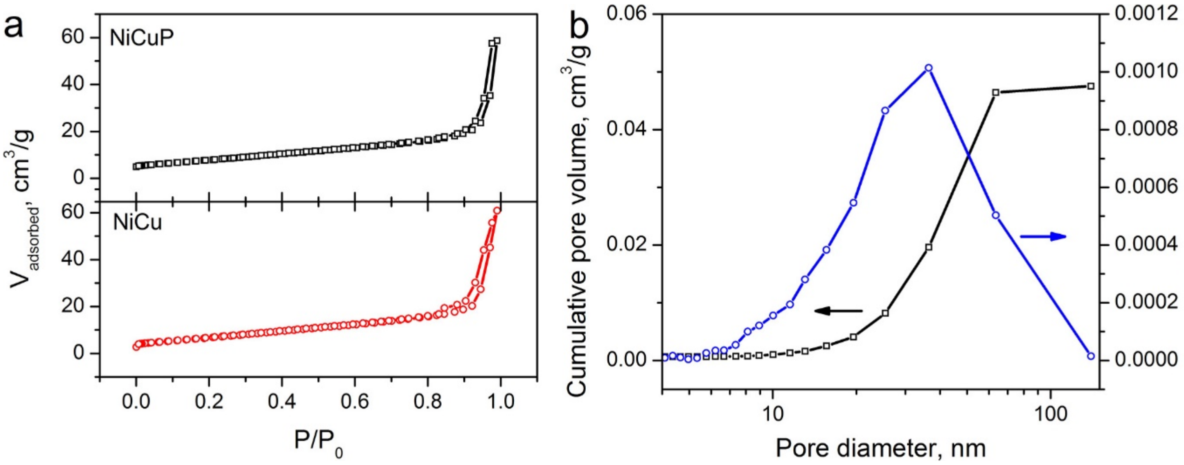

Figure S2. (a) Liquid N_2 physiosorption isotherms of NiCuPand NiCuP. (b) Pore volume and pore size distribution of NiCuP calculated from its physiosorption isotherm by the BJH method.

The deposited NiCu and NiCuP materials were scrapped from stainless steel foils. Their specific surface areas were determined from their liquid N_2 physisorption isotherms at 18.6 and 19.5 m^2/g, respectively. The pore size distribution of NiCuP was calculated by the BJH method, showing a wide pore size distribution centered at about 40 nm.

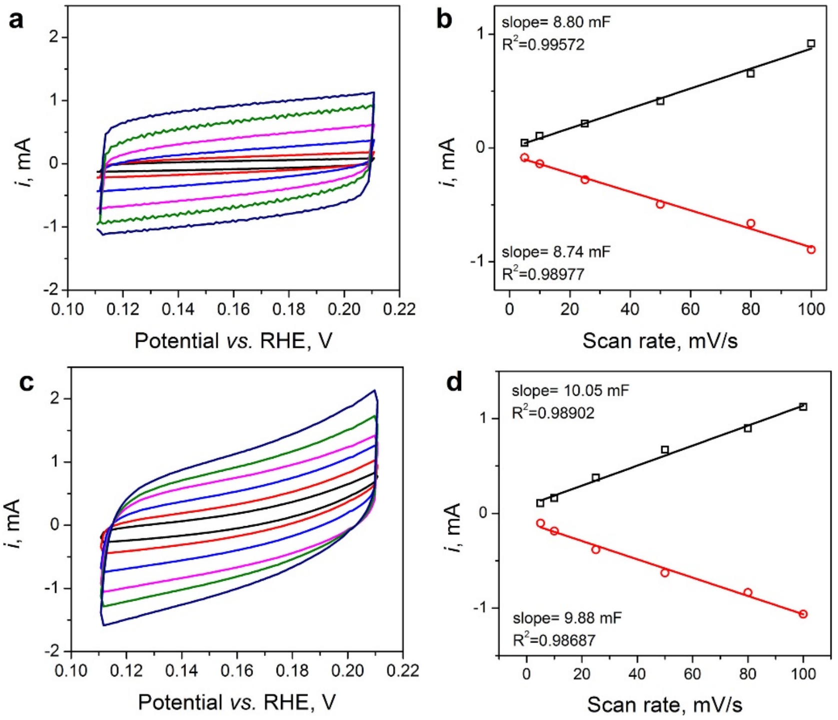

Figure S3. CV scans of (a) NiCu and (c) NiCuP in a non-Faradic region at different scan rates; linear fits of current densities at different scan rates of (c) NiCu and (d) NiCuP.

The surface roughness factor (RF) of the NiCu and NiCuP electrodes was estimated by measuring its electrochemically active surface area (ECSA) from its electrochemical double-layer capacitance (C_{dl}).[1, 2] Cyclic voltammogram (CV) scans of the electrodes in a non-Faradaic region in 0.1 M NaOH electrolyte at different scan rates (5 to 100 mV/s) are shown in Figure S2a. In the potential window where no Faradic reactions happen, the forward and backward CV scans were fitted with CV scan rates. The difference in the fitted slopes of forward and backward CV scans was used to determine the C_{dl}, which is 8.77 mF and 9.9 mF for the NiCu and NiCuP electrode, respectively. ECSA is then calculated by dividing the C_{dl} by the specific surface capacitance (C_s) of electrode surface as follows:

$$\mathrm{ECSA} = \frac{C_{dl}}{C_s} \quad (1)$$

A commonly used C_s value for metal surfaces (40 μF/cm^2) was used here.[1, 2] The ECSA of NiCu and NiCuP is estimated to be 219 and 247 cm^2, which give the RF of 438 and 494 for NiCu and NiCuP electrodes, respectively. It should be noted that the C_s value of metal phosphides is not available, and the choice of 40 μF/cm^2 may cause errors up to 20% or higher. However, SEM images (Figure S4) show that NiCu and NiCuP have similar structures. Further, the specific surface areas of NiCu and NiCuP determined by liquid N_2 physisorption (Figure S2) have minor differences. These two experimental results are consistent with the RF values determined for NiCu and NiCuP.

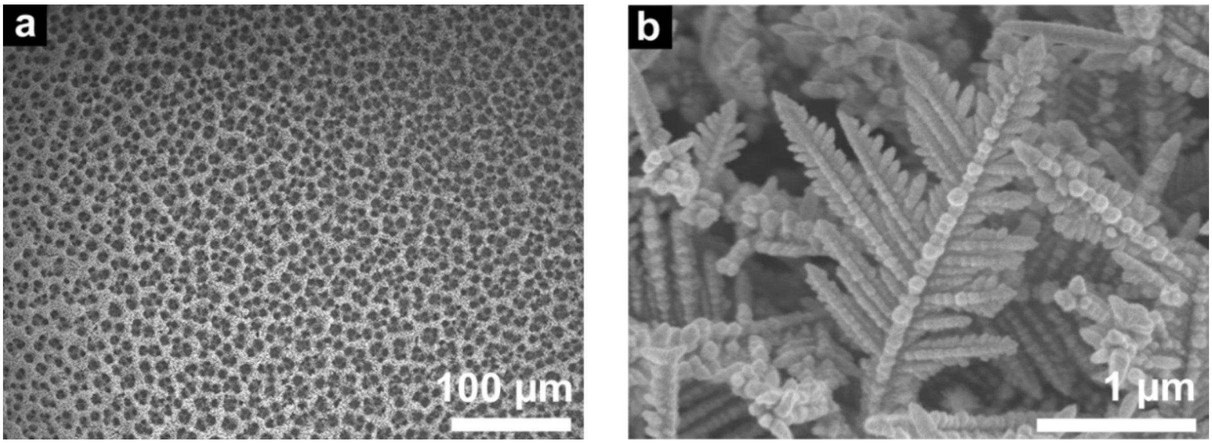

Figure S4. (a-b) SEM images of foamy NiCu alloys at different magnifications.

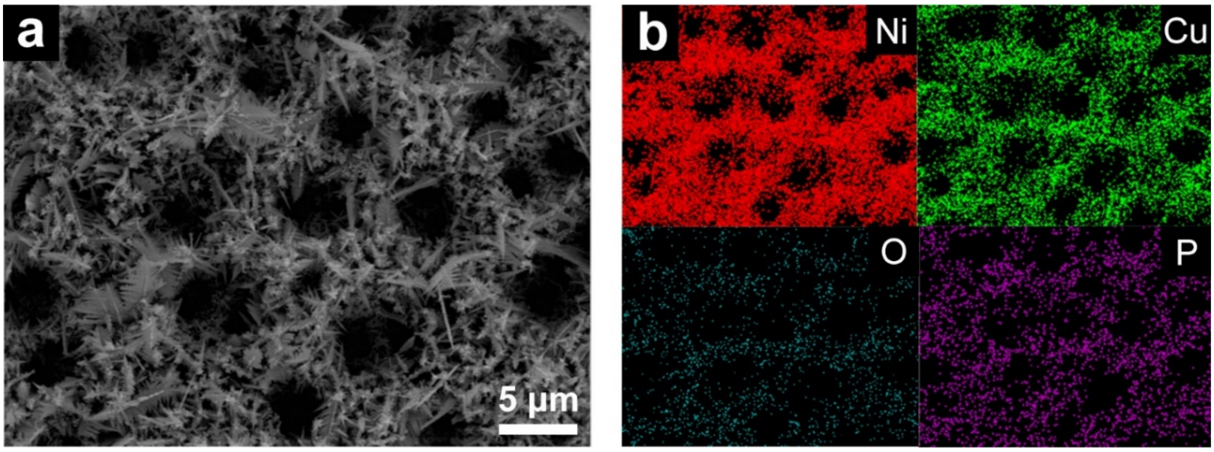

Figure S5. (a) SEM image and (b) the corresponding EDX maps of Ni, Cu, O, and P in NiCuP.

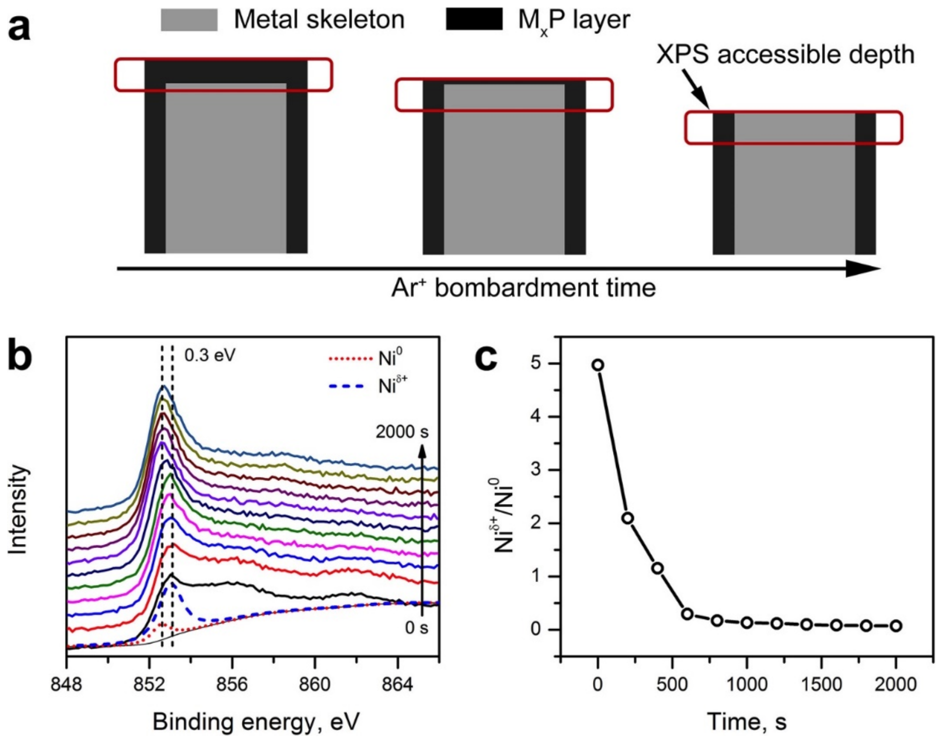

Figure S6. (a) Schematic illustration of phosphide layer removal from NiCuP under Ar^+ bombardment. (b) XPS depth profiles of NiCuP at Ni $2p_{3/2}$ edge. (c) Abundance ratio between Ni^0 and $Ni^{\delta+}$ extracted from XPS spectra in (b).

As illustrated in Figure S6a, the surface of NiCuP is gradually removed under Ar^+ bombardment. Because NiCuP has a highly porous structure, when the surface phosphide layer is removed, a small quantity of P presented on the sides of metal skeleton would always appear in the XPS spectra. Thus, it is difficult to directly determine the thickness of metal phosphide layer by monitoring XPS spectra at P edges. Instead, when the surface metal phosphide layer is removed, the XPS peaks from pure metal should become much stronger. This is confirmed in Figure S6b. The peak of Ni 2p 3/2 shifted from 853.0 to 852.7 eV under Ar^+ bombardment. This Ni feature can be split into two peaks: one from metallic Ni^0 (852.6 eV) in the metal skeleton of NiCu and the other from Ni_2P in the surface phosphide layer. Figure S6c shows that the $Ni^{\delta+}/Ni^0$ ratio quickly decreases at the beginning of the Ar^+ bombardment, and becomes unchanged after 1000 sec. Based on the etching rate of Ni (0.36 nm/min) reported in a previous study,[3] we can roughly estimate that the thickness of the surface phosphide layer in NiCuP is about 6 nm. This finding suggests that the low temperature phosphidization method is limited to the surface metal oxide layer of the NiCu deposits.

Table S1. HER performance comparison between NiCuP and recently reported bifunctional catalysts in alkaline media.

Catalysts	**Electrolyte**	***j*, mA/cm^2**	**η required, mV**	**Tafel slope, mV/dec**	**Ref.**
NiCuP	1 M KOH	50 100	–146 –216	47	this work
PCPTF	1 M KOH	30	–175	53	[2]
Co-P film	1 M KOH, 2000 rpm stirring	10 20 100	–94 –115 –158	42	[4]
CoP nanowire	1 M KOH	10	–209	129	[5]
Ni$_5$P$_4$ films	1 M KOH	10	–150	53	[6]
Ni$_2$P	1 M KOH	20	–205	N/A	[7]
MoB	1 M KOH	10	–225	59	[8]
Mo$_2$C	1 M KOH	10	–190	54	[8]
FeP/CC	1 M KOH	10	–218	146	[9]
NiCo alloy	1 M KOH	300	–410	120	[10]
np-CuTi	0.1 M KOH	10	–50	107	[11]
Ni$_{2/3}$Fe$_{1/3}$-rGO	1 M KOH	10	~–560	210	[12]
FeS$_x$/FeO$_x$	0.1 M KOH	10	–360	N/A	[13]
NiCoO/NiCoS	1 M KOH	10	–88	118	[14]
Ni@NC	1 M KOH	10	–190	N/A	[15]

Table S2. OER performance comparison between Ni-Cu-P and recently reported bi-functional catalysts in alkaline media.

Catalysts	**Electrolyte**	***j*, mA/cm^2**	**η required, mV**	**Tafel slope, mV/dec**	**Ref**
NiCuP	1 M KOH	10	292	49	This work
$NiFeO_x$ film	1 M KOH	10	~350	N/A	[1]
$NiCoO_x$ film	1 M KOH	10	~375	N/A	[1]
$NiCuO_x$ film	1 M KOH	10	~410	N/A	[1]
PCPTF	1 M KOH	30	330	53	[2]
Co-P film	1 M KOH, 2000rpm stirring	10	345	47	[4]
Ni_5P_4 films	1 M KOH	10	290	N/A	[6]
$Ni_{2/3}Fe_{1/3}$-rGO	1 M KOH	10	230	42	[12]
FeS_x/FeO_x	0.1 M KOH	10	450		[13]
NiCoO/NiCoS	1 M KOH	10	420	60	[14]
Ni@NC	1 M KOH	10	390	40	[15]
NiCu	30% KOH	145	300	55	[16]
NiFe	1 M KOH	10	215	28	[17]
NiCoO	1 M KOH	10	325	39	[18]
Ni_2P nanoparticles	1 M KOH 300 rpm stirring	10	290	59	[19]
Ni_2P nanowires	1 M KOH 300 rpm stirring	10	330	47	[19]
a-Co_2B	1 M KOH	10	380	45	[20]

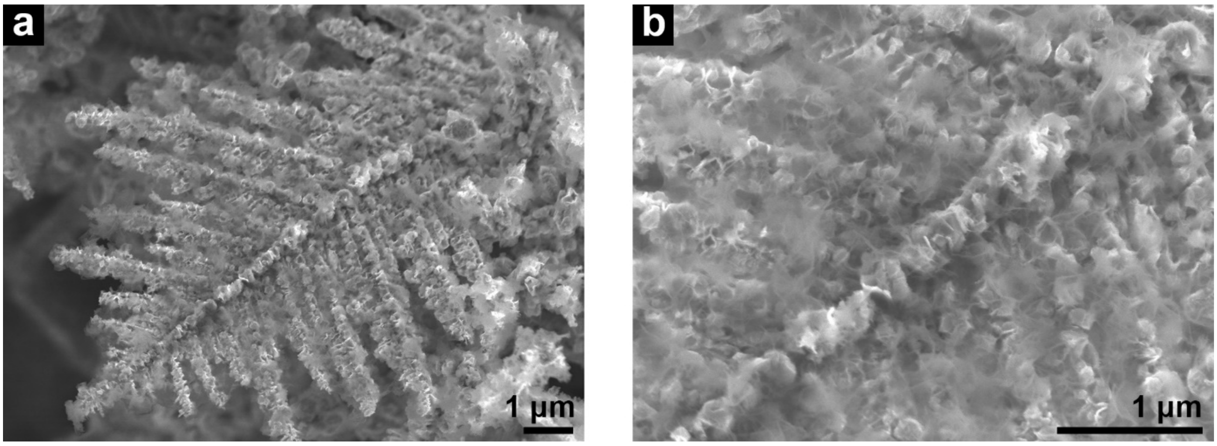

Figure S7. SEM images NiCuP after a 120-h OER test at 50 mA/cm^2 at different magnifications.

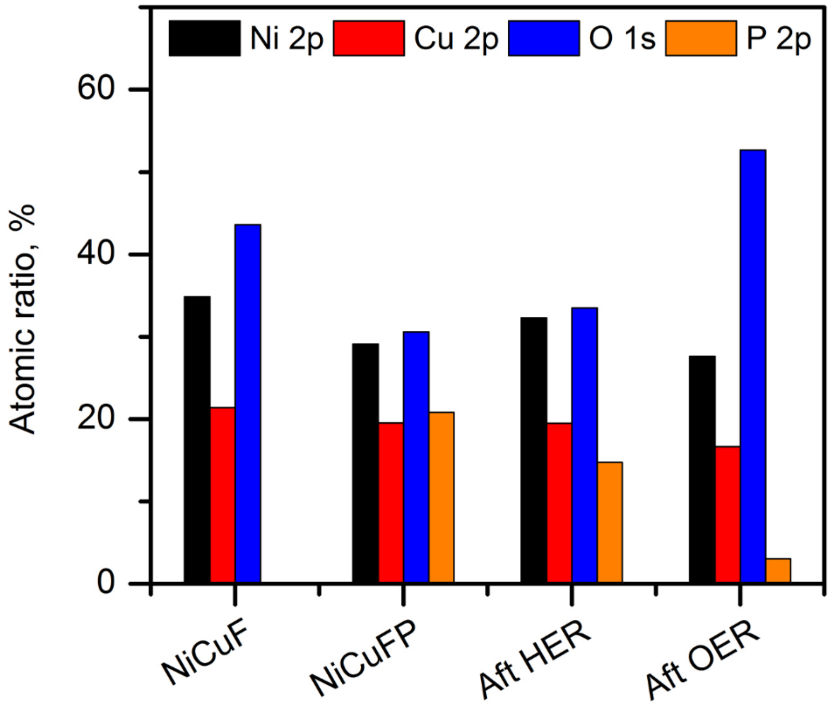

Figure S8. The elemental abundances of Ni, Cu, O and P quantified by XPS for Ni-Cu and Ni-Cu-P (before and after 120-h HER and OER tests). Note that the ratio of Ni and Cu is almost constant (~1:0.56) for all samples.

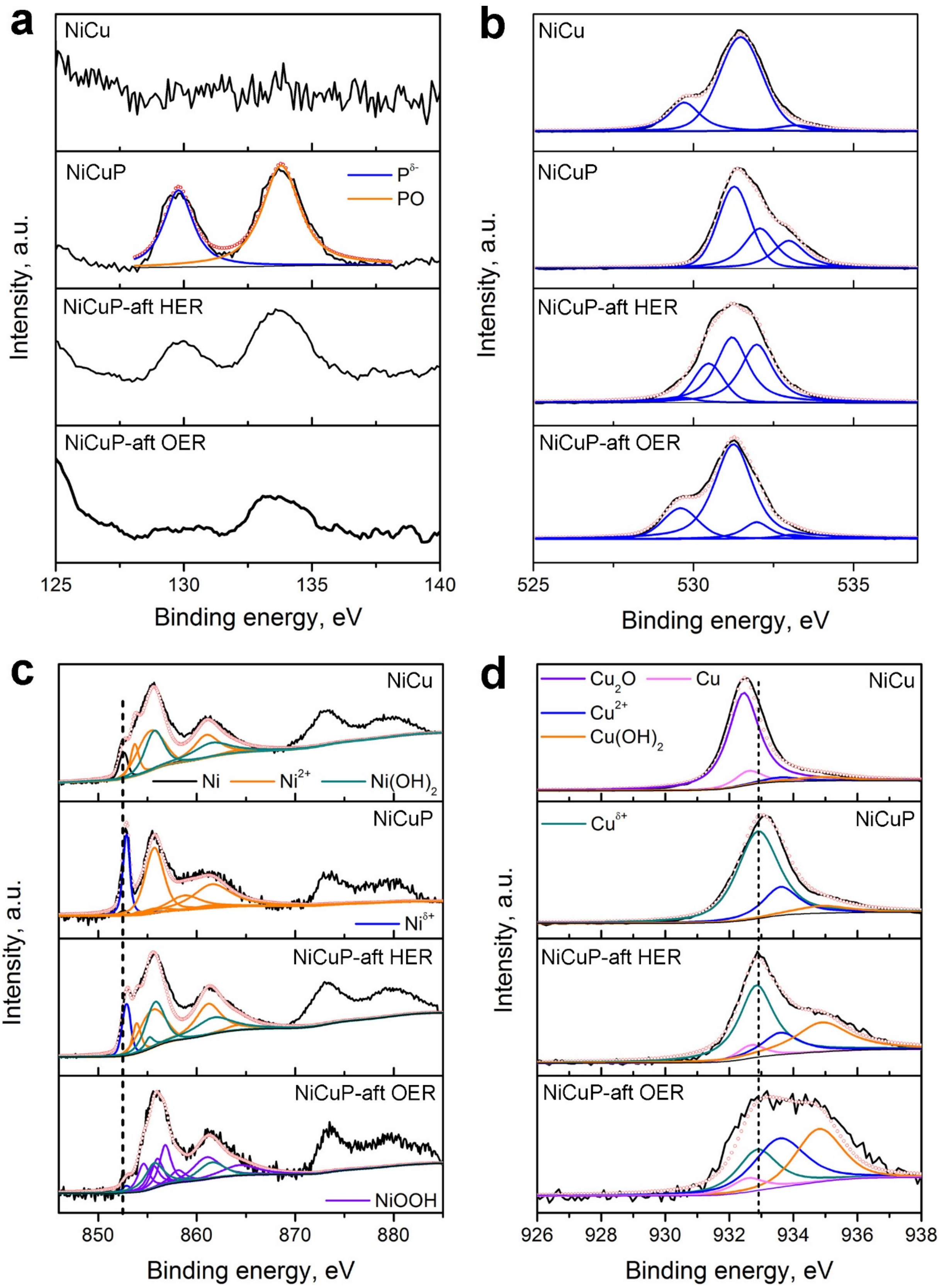

Figure S9. High-resolution XPS scans of (a) P, (b) O, (c) Ni, and (d) Cu of NiCu and NiCuP before and after 120-h HER and OER tests performed in 1 M KOH.

Figure S9a shows that no P is detected in NiCu. After NaH_2PO_2 treatment, there are two P 2p peaks at ~129.6 and ~134.2 eV in NiCuP, which can be assigned to $P^{\delta-}$ in metal phosphides and P-O bond in phosphates, respectively.[2] After 120-h HER and ORE tests, the phosphide P features become weaker.

In XPS spectra near O edge (Figure S9b), O peaks from metal oxides at ~292.5 eV and O-H bonds at ~531 eV can be observed in NiCu. After NaH_2PO_2 treatment, these features are replaced with three new peaks at ~531.3, ~532.1, and ~533 eV, which can be assigned to P-O bonds.[21] After HER test, metal oxide and –OH features reappear together with the decrease of P-O features. After OER test, most O atoms are bonded with –OH, and the rest O atoms are bonded with metals and P.

The assignment of Ni 2p 3/2 features in Figure S9c was performed following two previous studies.[22, 23] Metallic Ni (852.6 eV), NiO (853.7, 855.4 and 860.9 eV), and $Ni(OH)_2$ (855.7 and 861.5 eV) can be found in Ni-Cu. After NaH_2PO_2 treatment, $Ni^{\delta+}$ from Ni_2P at 852.9 eV can be identified in Ni-Cu-P. The features from $Ni(OH)_2$ are not visible. The remaining Ni^{2+} features can be assigned to Ni phosphate. After HER test, $Ni(OH)_2$ peaks appear again, while the intensity of peaks from Ni_2P decreases. After OER test, several new Ni peaks from NiOOH (854.6, 856.8 and 861.1 eV) emerge, and become the major Ni features. The peaks from Ni_2P become much weaker. This suggests the transformation of Ni(II) to Ni(III) during OER.

The Cu 2p 3/2 features in Figure S9d were assigned according to several previous studies.[24-26] Ni-Cu is partically covered by metal oxides, with several peaks from metallic Cu at 932.6 eV, Cu_2O at ~932.5 eV, CuO at 933.6 eV, and $Cu(OH)_2$ at 934.7 eV. After NaH_2PO_2 treatment, the peaks from Cu_2O and metallic Cu are replaced with a new peak of $Cu^{\delta+}$ from Cu_3P at 932.9 eV.[25] The peak intensity of Cu^{2+} also increased, due to the formation of Cu phosphates. After the 120-hours HER test, $Cu^{\delta+}$ peak indensity decreased, while the peak intensity of $Cu(OH)_2$ increased. After the 120-hours OER test, the peak intensity of Cu^{2+} and $Cu(OH)_2$ increases further.

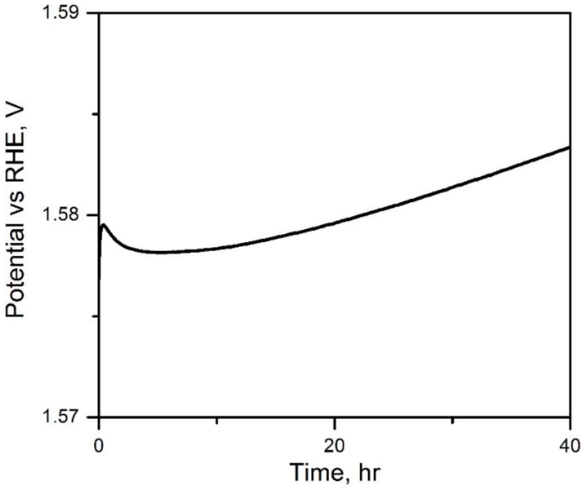

Figure S10. Chronopotentiometric responses of NiCuP in OER test at 50 mA/cm^2 in the first 40 h.

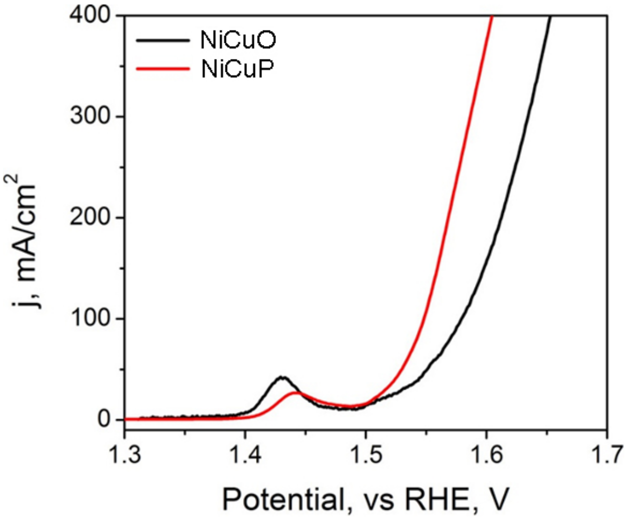

Figure S11. OER polarization LSV scan curves of Ni-Cu-O (Ni-Cu after passivation) and NiCuP. They were tested at the same condition.

Table S3. Performance comparison of recently reported bifunctional catalysts for total water splitting. Note that all values in this table are obtained in tests using a two-electrode configuration.

Catalysts	Electrolyte	*j*, mA/cm^2	Potential, V	Ref
NiCuP	1 M KOH	20.8	1.6	This work
Co phosphide/phosphate film	1 M KOH	10	1.6	[2]
Co-P film	1 M KOH, 2000 rpm	~4	1.63	[4]
FeS_x/FeO_x	0.1 M KOH	10	2	[13]
NiCoO/NiCoS	1 M KOH	5	1.65	[14]
a-Co_2B	1 M KOH	10	1.61	[20]
NiSe nanowire	1 M KOH	10	1.63	[27]
NiCoFe LDH	1 M KOH	10	1.62	[28]

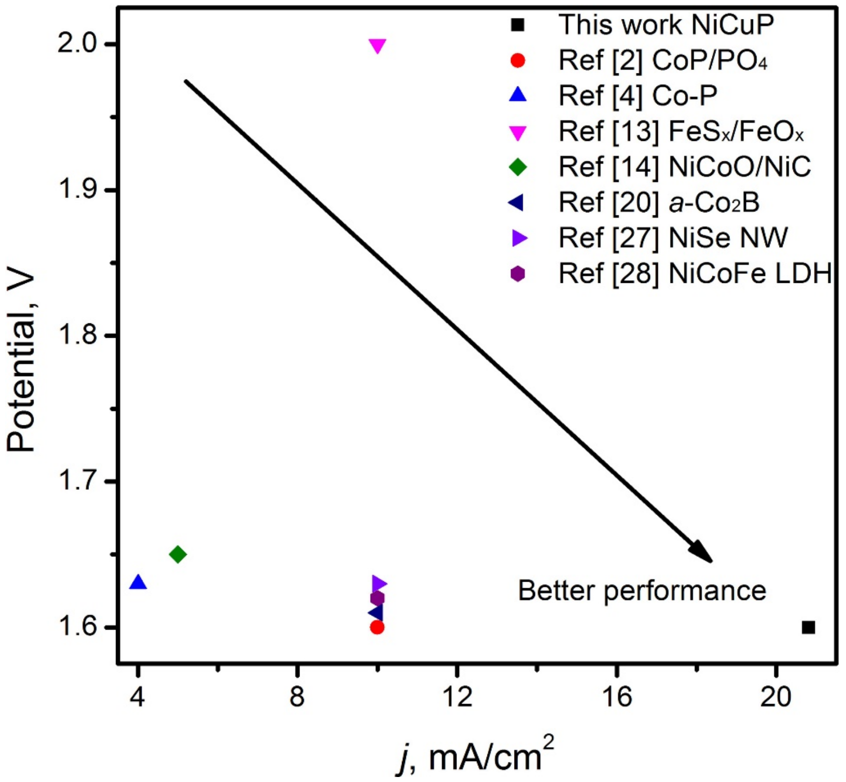

Figure S12. Performance comparison of various bifunctional electrocatalysts for total water splitting.

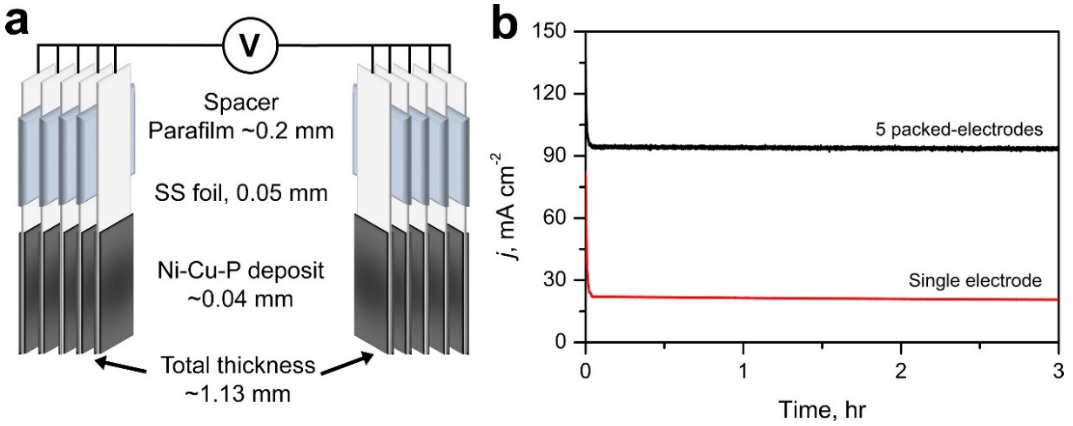

Figure S13. (a) Schematic illustration of stacking five pieces of NiCuP electrodes to form a packed electrode. (b) Recorded current density of the two-electrode water electrolyser using packed and single electrodes for 3 hours in 1 M KOH electrolyte.

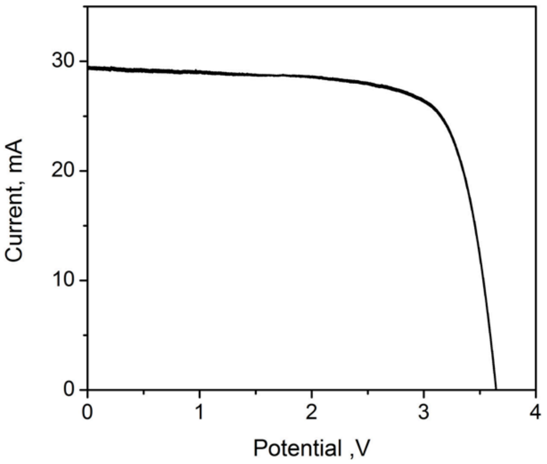

Figure S14. Current-voltage curve of the flexible Si solar cell used in this study with an open-circuit voltage (V_{oc}) of 2 V and a photoconversion efficiency of 6% connected in series under the illumination of a solar simulator. As estimated from the measurement, the V_{oc} for each panel could reach about 1.82 V.

The efficiency (η) of the electrolyzer was calculated according to a previous reported method[29] by the equation below:

$$\eta = \frac{2\times 1.23\ (\mathrm{V})\times \mathrm{N_{H2}}(\mathrm{mol})\times 96485(\mathrm{C\cdot mol^{-1}})}{\mathrm{I}(\mathrm{W\cdot cm^{-2}})\times \mathrm{A}(\mathrm{cm^{2}})\times \mathrm{t}(\mathrm{sec})}\times 100\%$$

The amount of H_2 produced was quantified by the GC. I is the intensity of the light source. A is the area of the solar panel; and t is the illumination time.

References cited in the ESI

[1] McCrory, C. C. L.; Jung, S.; Peters, J. C.; Jaramillo, T. F., *J. Am. Chem. Soc.,* **2013**, *135*, 16977.
[2] Yang, Y.; Fei, H.; Ruan, G.; Tour, J. M., *Adv. Mater.,* **2015**, *27*, 3175.
[3] Cao, Y.; Nyborg, L., *Surf. Interface Anal.,* **2006**, *38*, 748.
[4] Cheng, Y.; Xu, C.; Jia, L.; Gale, J. D.; Zhang, L.; Liu, C.; Shen, P. K.; Jiang, S. P., *Appl. Catal., B,* **2015**, *163*,
[5] Tian, J.; Liu, Q.; Asiri, A. M.; Sun, X., *J. Am. Chem. Soc.,* **2014**, *136*, 7587.
[6] Ledendecker, M.; Krick Calderón, S.; Papp, C.; Steinrück, H.-P.; Antonietti, M.; Shalom, M., *Angew. Chem. Int. Ed.,* **2015**, *54*, 12361.
[7] Popczun, E. J.; McKone, J. R.; Read, C. G.; Biacchi, A. J.; Wiltrout, A. M.; Lewis, N. S.; Schaak, R. E., *J. Am. Chem. Soc.,* **2013**, *135*, 9267.
[8] Vrubel, H.; Hu, X., *Angew. Chem. ,* **2012**, *124*, 12875.
[9] Liang, Y.; Liu, Q.; Asiri, A. M.; Sun, X.; Luo, Y., *ACS Catal.,* **2014**, *4*, 4065.
[10] Lupi, C.; Dell'Era, A.; Pasquali, M., *Int. J. Hydrogen Energy,* **2009**, *34*, 2101.
[11] Lu, Q.; Hutchings, G. S.; Yu, W.; Zhou, Y.; Forest, R. V.; Tao, R.; Rosen, J.; Yonemoto, B. T.; Cao, Z.; Zheng, H.; Xiao, J. Q.; Jiao, F.; Chen, J. G., *Nat. Commun.,* **2015**, *6*, 6567.
[12] Ma, W.; Ma, R.; Wang, C.; Liang, J.; Liu, X.; Zhou, K.; Sasaki, T., *ACS Nano,* **2015**, *9*, 1977.
[13] Martindale, B. C. M.; Reisner, E., *Adv. Energy Mater.,* **2016**, *6*, 201502095.
[14] Peng, Z.; Jia, D.; Al-Enizi, A. M.; Elzatahry, A. A.; Zheng, G., *Adv. Energy Mater.,* **2015**, *5*, 201402031.
[15] Ren, J.; Antonietti, M.; Fellinger, T.-P., *Adv. Energy Mater.,* **2015**, *5*, 201401660.
[16] Fazle Kibria, A. K. M.; Tarafdar, S. A., *Int. J. Hydrogen Energy,* **2002**, *27*, 879.
[17] Lu, X.; Zhao, C., *Nat. Commun.,* **2015**, *6*, 6616.
[18] Yang, Y.; Fei, H.; Ruan, G.; Xiang, C.; Tour, J. M., *ACS Nano,* **2014**, *8*, 9518.
[19] Stern, L. A.; Feng, L. G.; Song, F.; Hu, X. L., *Energy Environ. Sci.,* **2015**, *8*, 2347.
[20] Masa, J.; Weide, P.; Peeters, D.; Sinev, I.; Xia, W.; Sun, Z.; Somsen, C.; Muhler, M.; Schuhmann, W., *Adv. Energy Mater.,* **2016**, *6*, 201600980.
[21] Brow, R. K., *J. Non-Cryst. Solids,* **1996**, *194*, 267.
[22] Biesinger, M. C.; Payne, B. P.; Lau, L. W. M.; Gerson, A.; Smart, R. S. C., *Surf. Interface Anal.,* **2009**, *41*, 324.
[23] Elsener, B.; Atzei, D.; Krolikowski, A.; Rossi, A., *Surf. Interface Anal.,* **2008**, *40*, 919.
[24] Khattak, G. D.; Salim, M. A.; Wenger, L. E.; Gilani, A. H., *J. Non-Cryst. Solids,* **2000**, *262*, 66.
[25] Tian, J.; Liu, Q.; Cheng, N.; Asiri, A. M.; Sun, X., *Angew. Chem. Int. Ed.,* **2014**, *53*, 9577.
[26] Gerken, J. B.; McAlpin, J. G.; Chen, J. Y. C.; Rigsby, M. L.; Casey, W. H.; Britt, R. D.; Stahl, S. S., *J. Am. Chem. Soc.,* **2011**, *133*, 14431.
[27] Tang, C.; Cheng, N.; Pu, Z.; Xing, W.; Sun, X., *Angew. Chem. Int. Ed.,* **2015**, *54*, 9351.
[28] Zhu, X.; Tang, C.; Wang, H.-F.; Li, B.-Q.; Zhang, Q.; Li, C.; Yang, C.; Wei, F., *J. Mater. Chem. A,* **2016**, *4*, 7245.
[29] Liu, C.; Tang, J.; Chen, H. M.; Liu, B.; Yang, P., *Nano Lett.,* **2013**, *13*, 2989.